

Article

The Effects of Post-Welding Heat Treatment on the Cryogenic Absorbed Energy of High Manganese Steel Weld Metal

Seungho Baek ^{1,2}, Minha Park ^{1,2}, Je In Lee ^{1,*}  and Sung-Hwan Kim ^{2,*} 

¹ Department of Materials Science and Engineering, Pusan National University, Busan 46241, Republic of Korea; qor3154@kitech.re.kr (S.B.); pmh0812@kitech.re.kr (M.P.)

² Dongnam Regional Division, Korea Institute of Industrial Technology, Busan 46938, Republic of Korea

* Correspondence: jilee@pusan.ac.kr (J.I.L.); dashwan@kitech.re.kr (S.-H.K.); Tel.: +82-51-510-2383 (J.I.L.); +82-51-309-7417 (S.-H.K.)

Abstract: In this study, a post-weld heat treatment (PWHT) was proposed at high temperatures of 600 °C, 750 °C, and 900 °C for 30 min to significantly improve the impact absorbed energy of high manganese steel weld metal. Electron backscatter diffraction (EBSD), electron probe microanalysis (EPMA), and high-angle annular dark field scanning transmission electron microscopy (HAADF-STEM) were employed to characterize the production and study the deformation mechanisms in the high manganese steel weld metal. The impact absorbed energy is divided into crack initiation energy and crack propagation energy, which are divided by the value of P_{max} . The cryogenic impact absorbed energy was 81 J. After PWHT at 600 °C, 750 °C, and 900 °C, it was 75 J, 69 J, and 88 J, respectively. The impact absorbed energies did not follow a proportional relationship with the PWHT temperatures. The increase in impact absorbed energy can be attributed to the narrowing of the dendritic region, which blocks the crack propagation path and efficiently prevents crack propagation. Conversely, the decrease in impact absorbed energy can be attributed to the presence of 100-nm-sized $(Cr, Mn)_{23}C_6$ -type carbides at the grain boundaries, which facilitate crack propagation.

Keywords: high manganese steel; weld metal; stacking fault energy; post-welding heat treatment; cryogenic impact absorbed energy



Citation: Baek, S.; Park, M.; Lee, J.I.; Kim, S.-H. The Effects of Post-Welding Heat Treatment on the Cryogenic Absorbed Energy of High Manganese Steel Weld Metal. *Metals* **2023**, *13*, 1126. <https://doi.org/10.3390/met13061126>

Academic Editor: Jiehua Li

Received: 16 May 2023

Revised: 6 June 2023

Accepted: 13 June 2023

Published: 15 June 2023



Copyright: © 2023 by the authors. Licensee MDPI, Basel, Switzerland. This article is an open access article distributed under the terms and conditions of the Creative Commons Attribution (CC BY) license (<https://creativecommons.org/licenses/by/4.0/>).

1. Introduction

Recently the demand for cryogenic materials has increased due to the increasing demand for Liquefied Natural Gas (LNG) and liquefied hydrogen, and this has attracted considerable research interest. In particular, studies on austenitic high manganese steel, which are economical and have excellent strength compared to existing cryogenic materials, are being actively conducted [1,2]. However, high manganese steel has the disadvantage of lower cryogenic toughness than other cryogenic materials such as 9% nickel steel and stainless steel.

Austenitic high manganese steel has been extensively studied for its excellent mechanical properties based on the transformation-induced plasticity (TRIP) and twinning-induced plasticity (TWIP) effects [3–5]. The TRIP and TWIP effect are closely related to the stacking fault occurring in the material, which is the main deformation mechanism of high manganese steel. When the SFE of a high manganese steel is above 20 mj/m^2 , the deformation twin becomes the main deformation mechanism during deformation, resulting in improved material properties through the twinning-induced plasticity (TWIP) effect. When the SFE is below 20 mj/m^2 , the transformation-induced plasticity (TRIP) effect becomes dominant during deformation and the ϵ -martensite and α' -martensite phase transformations act as the main deformation mechanisms [6]. Therefore, it is important to understand the main deformation behavior of high manganese steel through SFE calculation. Moreover, it is important to fully understand the properties of each element in high manganese steel and to know their effects on the mechanical properties of high manganese steel. In binary

Fe-Mn alloys, low concentrations (10–16 at.%) of manganese reduce the SFE, but in the concentration range 16~33 at.%, manganese increases the SFE by 18 mj/m² per 1 at%. In a previous paper Kang performed short-range ordering (SRO) to investigate the Mn-C interaction. The stress required for SRO failure was calculated by ab initio calculation, a free energy reduction of 0.0528 eV (or 5.09 kJ/mol) per manganese atom was reported, and the Mn-C interaction was found to be important [7]. The effect of chromium is similar to that of manganese and chromium located in stacking faults reduces the SFE by 1.7 mj/m². In addition, chromium interactions between chromium atoms favor Cr-Fe bond formation rather than Cr-Cr bond formation. Furthermore, when carbon and manganese are present, C-C bonds must be considered [8]. Interstitial carbon has the greatest influence in high manganese steel. Carbon increases lattice parameters and improves the stability of austenite rather than martensite. Carbon is an interstitial atom in crystals, so its diffusion rate is higher than that of other atoms. In other words, carbon can easily occupy interstitial sites within the crystal structure and due to this property, it has a higher diffusion rate compared to other atoms. Experimental evidence for the short-range diffusion of carbon was reported by Hickel et al., who observed an increase in the width of stacking faults by 40–60% through transmission electron microscopy, as the stacking fault energy decreased by 9 mj/m² [9]. Recently, when investigating the deformation behavior of high manganese steel, most of the existing literature has focused on its tensile strength and its correlation with work hardening [10–12]. However, research on impact absorbed energy is still insufficient considering its importance. Impact absorbed energy represents the amount of energy absorbed by the material immediately after impact and during crack propagation, indicating its resistance to fracture [13]. Impact absorbed energy is divided into crack initiation energy for crack initiation and crack propagation energy, which is the energy absorbed during cracking. Therefore, it is important to distinguish between crack initiation energy and crack propagation energy to identify the main deformation mechanisms.

When conducting research on welded metals, it is important to consider the composition, weldability, and welding method [14]. Furthermore, it is crucial to understand the relationship between the welding methods and mechanical properties [15]. Since welding is necessary to make cryogenic structures using high manganese steel, research on high manganese steel weld metal is essential. Generally, weld metal has lower toughness due to its different characteristics from casting structure and rapid cooling compared to the base metal [16]. Previous studies have shown high manganese steel has a higher coefficient of thermal expansion and a lower thermal conductivity [17]. During welding, manganese loss occurs due to the vapor pressure of manganese; so, the microstructure of cast high manganese steel consists of well-developed dendrite and equiaxed grain. Well-developed dendrites can have a negative effect on mechanical properties, so to prevent this issue and improve corrosion resistance, tensile strength, and toughness of the weld metal, PWHT is a representative process [18]. In previous research, the influence of PWHT on high manganese steel was investigated, and it was found that by activating the TRIP and TWIP mechanisms, the ductility strength was improved. Furthermore, toughness was increased through a reduction in the partial dislocation density, and the properties were enhanced through microstructure control [19,20]. In the case of PWHT of high manganese steel, precipitation occurs and the microstructure is homogenized as the temperature increases [21]. Therefore, it is important to analyze and predict the effects of microstructure, precipitation, and recrystallization in order to increase the toughness of high manganese steel.

In this study, PWHT was performed to improve the cryogenic toughness of high manganese steel weld metal. Furthermore, the correlation between the microstructure, SFE, and cryogenic impact absorbed energy before and after PWHT was investigated.

2. Materials and Methods

Table 1 shows the chemical compositions of the austenitic high manganese steel base metal and filler metal used in this study. A 13 mm thick hot-rolled high manganese steel

plate was obtained and UOE (U-ing, O-ing, Expansion) formed. Double-side welded by submerged arc weld (SAW) was used.

Table 1. Chemical compositions of the high manganese steel used in this study.

| wt.% | C | Mn | P | S | Si | Cr | Mo | Ni | Fe |
|--------|------|------|-------|--------|------|------|-------|-------|------|
| Base | 0.47 | 24.9 | 0.01 | 0.0008 | 0.28 | 3.15 | 0.008 | 0.024 | Bal. |
| Filler | 0.4 | 22 | 0.009 | 0.001 | 0.15 | 2.41 | 1.33 | 1.92 | Bal. |

The welding current, voltage, welding speed, and preheating temperature for the process are shown in Table 2. PWHT involved heating in air at 600, 750, or 900 °C for 30 min and cooling in water. The PWHT temperature and time were set considering partial recrystallization and precipitates [22,23].

Table 2. Welding parameters.

| Welding Process | Heat Input (KJ/cm) | Welding Current (A) | Welding Voltage (V) | Welding Speed (cm/min) |
|-----------------|--------------------|---------------------|---------------------|------------------------|
| SAW | 21–24 | 640–750 | 28 | 40 |

Figure 1 shows the location of the specimen fabrication on the pipe used in this study. To analyze the characteristics of high manganese steel weld metal, specimens for Charpy impact testing and tensile testing were fabricated from the weld metal. The Charpy impact test specimens for the high manganese steel weld metal were fabricated according to ASTM E23 (10 mm × 10 mm × 55 mm, V-notch). The cryogenic impact absorbed energy was calculated automatically. Specifications and impact tests were performed in the temperature from −196 °C to 25 °C with an automatic ZWICK impact test machine (Ulm, Germany) with a 750 J capacity. Measurements were taken three times for each PWHT temperature condition and the V-notch was machined to be centered in the weld metal. The cryogenic impact absorbed energy is represented in the area obtained by multiplying the displacement value and the load. Crack initiation and crack propagation are segmented based on the P_{max} values of instrumented the Charpy impact test data [18]. The tensile specimens of the high manganese weld metal were prepared as sub-size specimens of ASTM E8M and the strain rate was set at 1 mm/min. Tensile tests were conducted at −190 °C by spraying liquid nitrogen inside the cryogenic chamber. Yield strength, ultimate tensile strength, and elongation were measured in the cryogenic environment, and each condition of PWHT was tested three times.

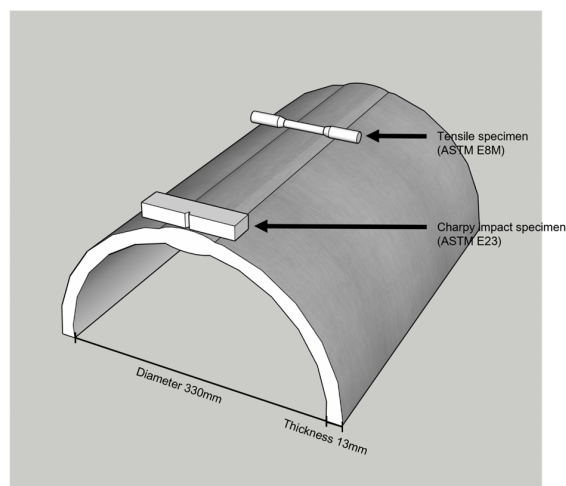


Figure 1. Locations of tensile and Charpy impact test specimens in the welded region of a submerged arc-welded high manganese steel pipe.

Specimens for electron probe microanalyzer analysis (EPMA) and electron backscatter diffraction (EBSD) were mechanically polished to 0.25 μm and then polished with colloidal silica. To observe the EBSD of the fracture surfaces, the fracture surfaces were heated in (90 vol.%) distilled water containing (10 vol.%) nickel plating solution at 85–90 $^{\circ}\text{C}$ for 2 h and then polished with colloidal silica. The EBSD data were analyzed using the OIM analysis program. Inverse pole figure (IPF), phase map, $\Sigma 3$ coincidence site lattice (CSL) map, and Schmid factor map were also analyzed. The precipitates were observed by a high-angle annular dark field scanning transmission electron microscopy (HAADF-STEM) operating at 200 kV. Thin foils for TEM observations were prepared by jet polishing at 0 $^{\circ}\text{C}$ at 25 V and 60 mA in a solution of 90% acetic acid and 10% perchloric acid.

3. Results and Discussion

3.1. Cryogenic Mechanical Properties

Figure 2a shows the engineering strain-stress curves of high manganese steel weld metal by different PWHT temperatures is plotted in Figure 2a. Tensile testing at cryogenic temperatures showed that the as-welded weld metal had a strength of 1079 MPa and an elongation of 24.6%. After PWHT at 600 $^{\circ}\text{C}$ or 750 $^{\circ}\text{C}$, the tensile strength increased to 1134 and 1121 MPa, respectively, and elongation decreased by 21.5% and 21%. However, after PWHT at 900 $^{\circ}\text{C}$, the tensile strength was 1089 MPa and the elongation was 29.4%, an increase of 4.8%. However, when PWHT was performed at 900 $^{\circ}\text{C}$, the steel exhibited a strength of 1089 MPa and maintained an equivalent level of strength comparable to that before PWHT with 29.4% elongation, which was improved by 4.8% compared to before PWHT.

Figure 2b shows the impact absorbed energy values of the high manganese steel weld metal before and after PWHT. The standard deviation is plotted in the symbol area. The cryogenic impact absorbed energy at 25 $^{\circ}\text{C}$ was 132 J for the as-welded weld metal, 130 J PWHT at 600 $^{\circ}\text{C}$, 135 J PWHT at 750 $^{\circ}\text{C}$, and 132 J PWHT at 900 $^{\circ}\text{C}$, which were the almost the same as the impact absorbed energies regardless of the PWHT temperatures. However, this pattern changed from the temperature below -150 $^{\circ}\text{C}$. At -150 $^{\circ}\text{C}$, the impact absorbed energy by PWHT temperature was 90 J for the as-welded weld metal, 89 J PWHT at 600 $^{\circ}\text{C}$, 82 J PWHT at 750 $^{\circ}\text{C}$, but 101 J after PWHT at 900 $^{\circ}\text{C}$. At -196 $^{\circ}\text{C}$, the impact absorbed energies for different PWHT temperatures were 81 J for as-welded metal, and PWHT at 600 $^{\circ}\text{C}$ and PWHT at 750 $^{\circ}\text{C}$, the impact absorbed energies decreased to 75 J and 69 J, but increased to 88 J after PWHT at 900 $^{\circ}\text{C}$.

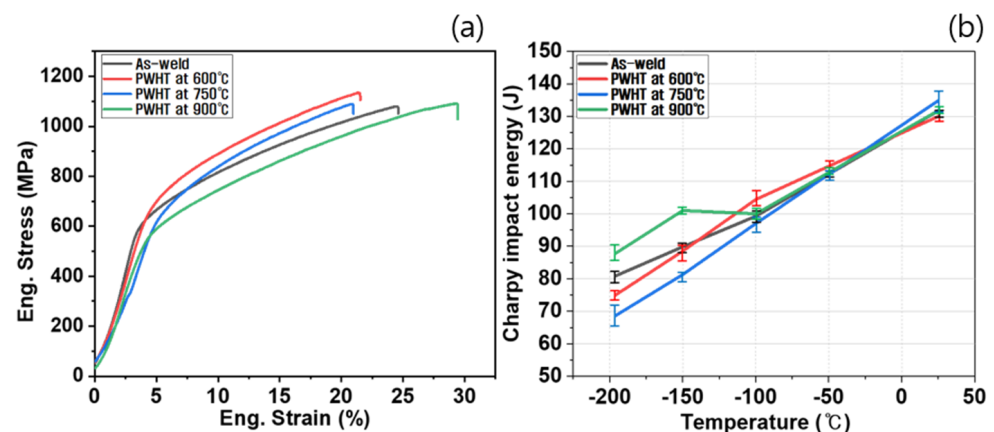


Figure 2. Mechanical properties of high manganese steel welded metal by different PWHT temperatures. (a) Strain-stress curves by different PWHT temperatures at -190 $^{\circ}\text{C}$ (b) Charpy impact test results at -196 – 25 $^{\circ}\text{C}$.

Figure 3 shows instrumented Charpy impact test results by PWHT temperature after Charpy impact testing at -196 $^{\circ}\text{C}$. The crack initiation energy (E_i) and the crack propagation energy (E_p) are obtained by calculating the areas below the load–displacement curves

divided by the maximum load (P_{max}). Unstable growth of the fracture is initiated force at the initiation of unstable crack propagation. This phase of the process is correlated with an abrupt reduction of the applied force accompanied by minimal increase in the displacement of force application point. After this moment, the effective fracture arrest begins and the sample undergoes plastic fracture [24]. In Figure 3, the crack initiation energies were (a) 19.6 J, (b), 21.0 J, (c) 18.7 J, and (d) 19.2 J, that is, crack initiation energy showed no significant dependence on the PWHT temperature. The corresponding crack propagation energies were (a) 61.4 J, (b) 54.0 J, (c) 48.3 J, and (d) 68.8 J. The crack propagation energies were highly dependent on the PWHT temperature.

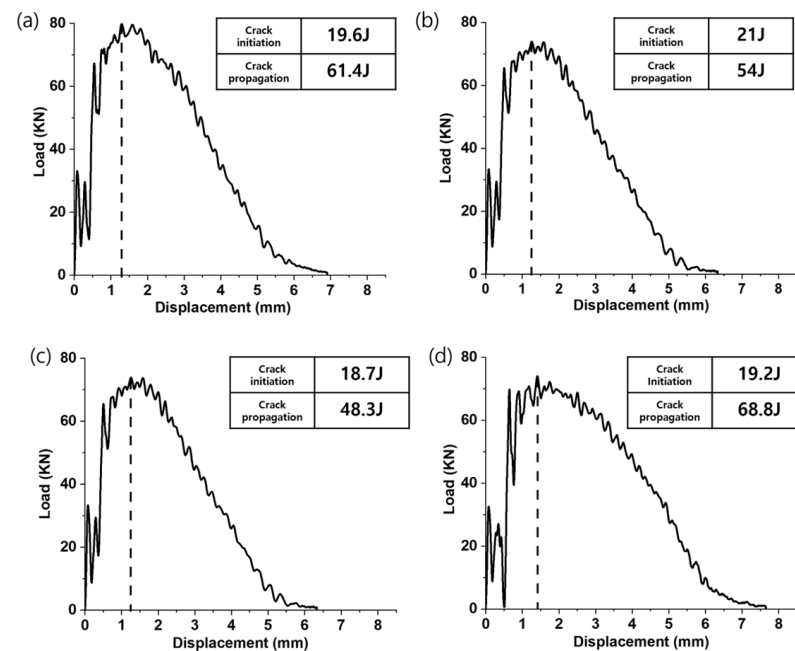


Figure 3. Instrumented Charpy impact test results for high manganese steel at different PWHT temperatures (a) As-welded, (b) PWHT at 600 °C, (c) PWHT at 750 °C, and (d) PWHT at 900 °C.

3.2. Microstructure

Figure 4a shows the second electron image of the high manganese steel weld metal before and after PWHT. As shown in Figure 4, the dendritic structure growing by the heat flow during solidification can be observed and no significant grain growth or recrystallization occurred after PWHT.

Figure 4b shows the EPMA analysis conducted to analyze the chemical composition and distribution differences between the inter-dendritic and dendritic regions. The average manganese content did not change drastically with the PWHT temperatures, which were (a) 17.6~24.2 wt.%, (b) 17~22.6 wt.%, (c) 17.7~24.3 wt.%, and (d) 16.6~21.3 wt.%. However, the deviation of manganese content in the inter-dendritic and dendritic regions decreased with increasing PWHT temperature, and manganese did not fully diffuse even at high PWHT temperatures due to its slow diffusion rate [25].

Notably, PWHT had a greater influence on crack propagation than crack initiation. The reason for this is as follows. At first, a ductile crack is formed at the center of the notch root after yielding and spreads laterally, acquiring full specimen width at the maximum load. Then the crack propagates into the width direction in tensile tear fracture mode even in the case of ductile fracture. The TWIP effect, which is the main deformation mechanism, is not significant when high manganese steel starts cracking. However, when the crack propagates, the TWIP effect spreads to the inside of the grain and has a great influence on the crack propagation energy.

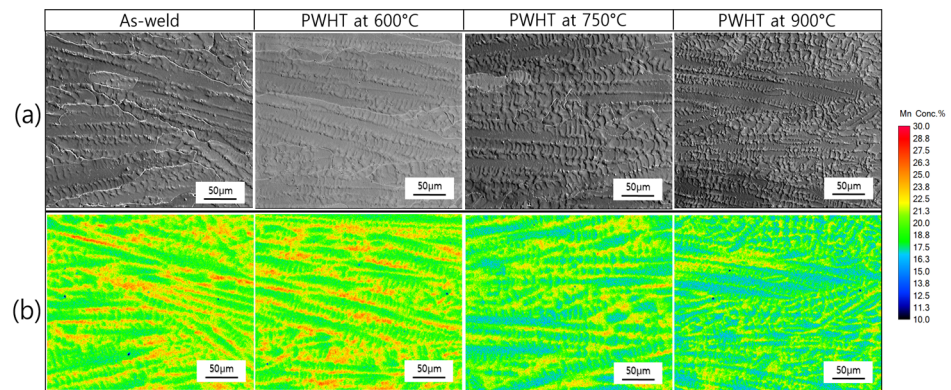


Figure 4. Secondary electron images and electron probe microanalyzer analysis manganese distribution maps of high manganese steel at different PWHT temperatures (a) Secondary electron images (b) electron probe microanalyzer analysis manganese distribution maps.

Figure 5 shows EBSD analysis of the high manganese steel before and after PWHT. High manganese steel has a high coefficient of thermal expansion and a lower thermal conductivity [18]. Therefore, high manganese steel is prone to internal thermal stresses during heat treatment compared to other types of steel. EBSD analysis was conducted to examine the effect of PWHT on the crystallographic orientation, as well as to determine the occurrence of deformation twinning, slip, and diffusionless transformation caused by thermal stress. Figure 5a shows the IPF map of the high manganese steel weld metal. The orientation of the inside of the grain before and after PWHT was the same and no twins or slips were observed. Previous studies have reported that partial recrystallization occurs in high manganese steel when annealed at 900 °C [26]. However, in this experiment, recrystallization did not occur despite PWHT up to 900 °C. The reason is that the driving force for recrystallization is low due to the low dislocation density inside the weld metal. However, the base metal exhibited a fully austenitic structure, and PWHT at 900, recrystallization occurred, resulting in an increase in grain size [27].

Figure 5b shows the phase map of the high manganese steel weld metal. The analysis results indicate that no phase transformation to ϵ -martensite or α' -martensite occurred before and after PWHT.

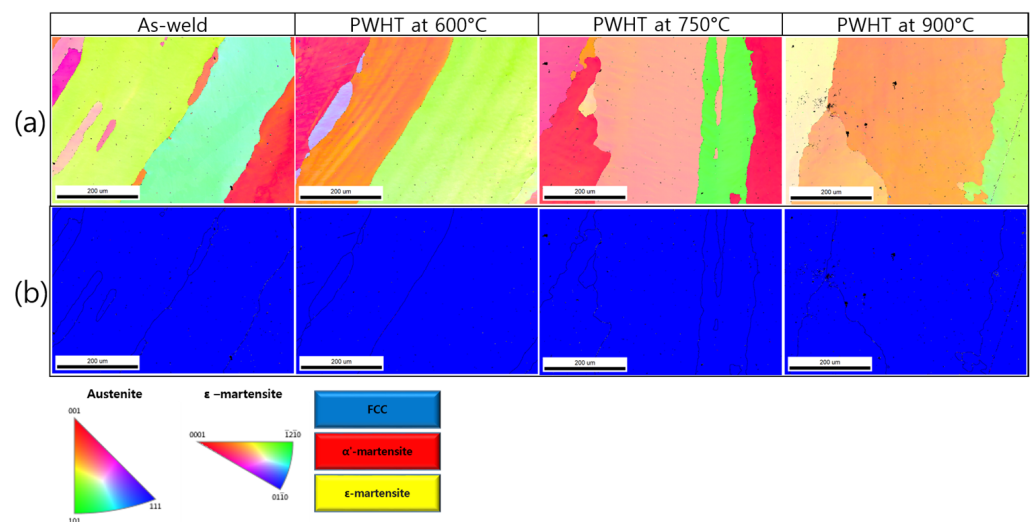


Figure 5. Inverse pole figure maps and phase maps of welded high manganese steel at different PWHT temperatures (a) Inverse pole figure map (b) phase map.

3.3. Stacking Fault Energy

The SFE according to the manganese, chromium, and carbon contents of the dendrite region and the inter-dendritic region was calculated using Equation (2).

$$\text{SFE} = 2\rho(\Delta G^{\gamma \rightarrow \varepsilon}) + 2\sigma^{\gamma/\varepsilon} \left(\text{mj/m}^2 \right) \quad (1)$$

The thermodynamic SFE calculation formula was used and the Fe-Mn-Cr-C based SFE calculation formula was used. The Olson-Cohen model was used and calculated after excluding the ΔG_{ex} value to exclude the effect on the coarse grain size of the weld metal [28–36].

Figure 6 shows a graph of the SFE values before and after PWHT. The SFE graph was scanned vertically along the 20 μm line on the EPMA mapping data image. SFE was (a) 15.8~24.8 mj/m^2 , (b) 16.5~24.6 mj/m^2 , (c) 15.2~22.8 mj/m^2 , and (d) 14.8~22 mj/m^2 . As the PWHT temperature increases, the difference in SFE values between inter-dendritic and dendrite regions decreases. The average width of the dendritic region is (a) 20.5 μm , (b) 20.5 μm , (c) 17.3 μm , and (d) 8.6 μm , and the width of the dendritic and inter-dendritic regions decreases due to the increase in the PWHT temperature. Not only does the SFE the deformation behavior but it also affects the critical resolved shear twinning stress. The critical resolved shear twinning stress can be expressed as follow [37].

$$\tau_t = \text{SFE}/Kbs \quad (2)$$

where τ_t = critical resolved shear twinning stress, SFE = stacking fault energy, K = fitting parameter, and bs = Burgers vector. Critical resolved shear twinning stress means the minimum critical resolved shear stress required for twinning to occur. The critical resolved shear twinning stress can separate a leading partial from a trailing partial and then create a twin embryo. As shown in the formula, SFE is proportional to τ_t . The calculation of SFE shows that the inter-dendritic region has a high τ_t , while the dendritic region has a low τ_t . Therefore, as welded, the wide dendritic region with low critical resolved shear twinning stress provides an easy path for crack propagation. PWHT, the average width of the inter-dendritic region gradually decreases from 20.5 μm to 8.6 μm , resulting in a narrower crack propagation path [38]. In addition, since the difference between the SFE values of the dendritic region and the inter-dendritic region is reduced, the impact absorbed energy is increased.

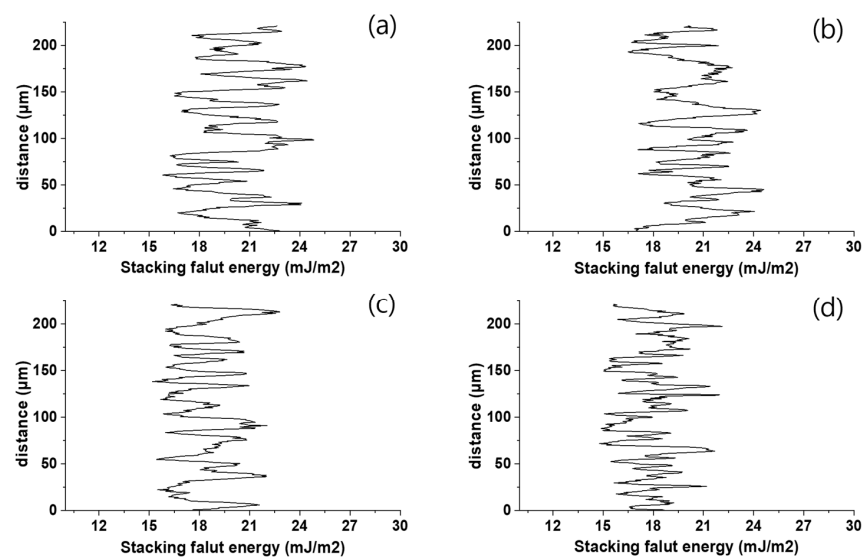


Figure 6. Plots of SFE values line scanned 1/2 thickness positions of welded metal by EPMA mapping data at different PWHT temperatures (a) As-welded, (b) PWHT at 600 °C, (c) PWHT at 750 °C, and (d) PWHT at 900 °C.

3.4. Precipitates

Figure 7 shows STEM images and TEM-EDX maps of the high manganese steel weld metal before and after PWHT. Alloy precipitates at grain boundaries tend to increase in size with longer exposure to elevated temperatures and longer duration [39]. The size of grain boundary precipitates is not uniform, and the deviation of the precipitate size differs by location.

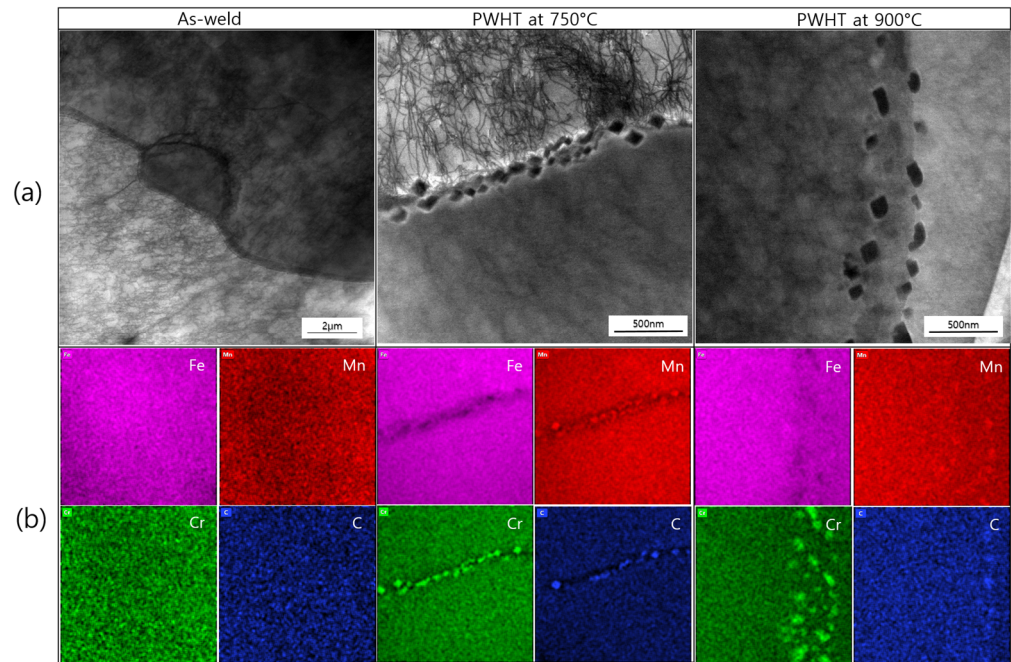


Figure 7. HAADF-STEM images and TEM-EDX maps of high manganese steel welded metal of at different PWHT temperature. (a) HAADF-STEM images (b) TEM-EDX maps.

In Figure 7a, no precipitates were observed at the grain boundaries before PWHT, whereas after PWHT, block-form carbides were formed at the grain boundaries. In Figure 7b,c, the average size of the precipitates was 100 nm and was not greatly affected by the PWHT temperature. Previous studies have reported that the carbides precipitated at the grain boundaries in high manganese steel were identified as $(\text{Cr}, \text{Mn})_{23}\text{C}_6$ type carbides [23]. As can be seen in Figure 2, manganese has a slower diffusion rate compared to other elements, resulting in a slower diffusion rate from the matrix to the grain boundary. This is why the diffusion of manganese from the matrix to the grain boundary is less than that of chromium. The negative effects of the precipitate on the impact absorbed energy can be summarized as follows. One reason is that the precipitation of the grain boundary can lead to the depletion of manganese and chromium. The depletion of manganese and chromium due to carbide precipitation reduces the SFE of the local area, which has a negative effect on impact toughness [40]. The second reason is that carbides can easily nucleate cracks, causing cracks to propagate along the grain boundary carbide particles during fracture. This leads to brittle failure rather than the TWIP effect during crack propagation in high manganese steel, which has a negative impact on the impact absorbed energy [41].

3.5. Analysis of Cryogenic Transformation Behavior

Figure 8 shows the fracture surfaces after the cryogenic Charpy impact test and (b) SEM-EDS analysis results of high manganese steel weld metal before and after PWHT. SEM-EDS analysis revealed non-metallic inclusions of Al_2O_3 . Gigacher et al. reported that various types of endogenous inclusions play an important role in ductile fracture processes [42]. Despite the presence of endogenous inclusions in high manganese steel weld metal, the fracture surface shows simply the characteristics of a fully ductile rup-

ture. Regardless of PWHT, all fracture surfaces were dimple fracture after the cryogenic impact test.

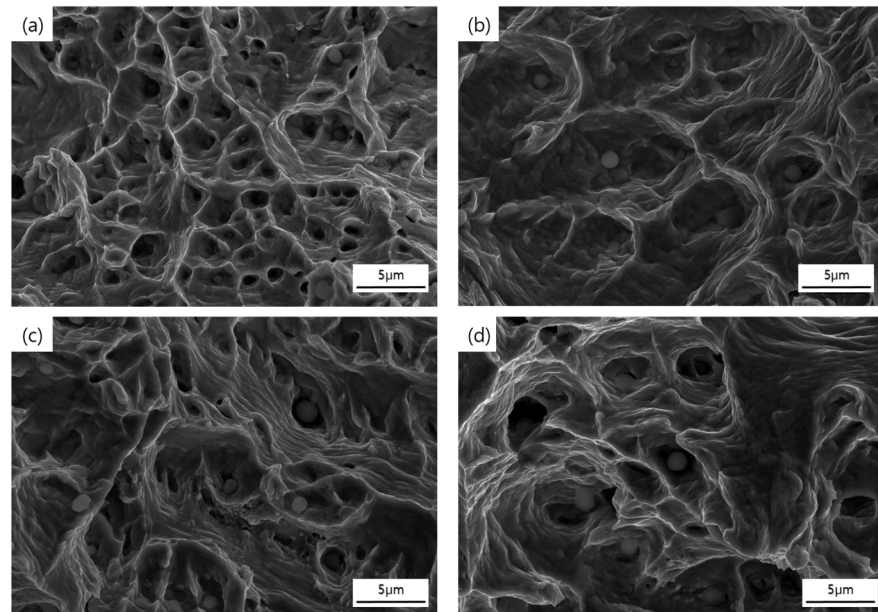


Figure 8. Fractography images of high manganese steel welded metal. (a) As-welded weld metal and after PWHT performed at (b) 600 °C, (c) 750 °C, and (d) 900 °C.

Figure 9 shows fracture surface $\Sigma 3$ CSL maps after cryogenic Charpy impact testing before and after PWHT. The green line is a $2\sim 15^\circ$ low angle boundary, the black line is a high angle boundary of $\geq 15^\circ$, and the red line is a twin boundary. As shown in Figure 9, slip and twinning were distributed inside the grains regardless of the PWHT, indicating that the TWIP effect acted as the main deformation behavior. However, the distribution and proportion of twinning and slip varied depending on the PWHT temperature. The as-welded fracture surface showed that slip and twinning were formed near the fracture surface after the cryogenic impact test, and stresses were not dispersed into the grains. However, as the PWHT temperature increased, slip and twinning were formed inside the grains, indicating that stress was dispersed inside the grains. In Figure 4 the SFE calculation results showed that the dendritic region had a lower critical resolved shear twinning stress value compared to the inter-dendritic region, and the relatively low critical resolved shear twinning stress in the inter-dendritic region served as a facile crack propagation path, leading to a decrease in impact absorbed energy. Before PWHT, the width of the dendritic region was 20.5 μm , which made crack propagation easier, and as a result, twinning and slip were not dispersed into the grain during crack propagation. After PWHT, the reduction in the average width of the dendritic region contributed to an increase in the impact absorbed energy by blocking the crack propagation paths and as a result, twinning and slip were dispersed into the grain during crack propagation.

Figure 10 shows a fracture surface Schmid factor maps after cryogenic Charpy impact testing before and after PWHT. Sigma value = $\begin{pmatrix} 0 & 0 & 0 \\ 0 & 0 & 0 \\ 0 & 0 & 0 \end{pmatrix}$ and the $\{111\}\langle 110\rangle$ slip system has been identified as the easiest slip system to activate in FCC crystals. The Schmid factor Sigma value (σ) is an index that represents the orientation of a specific plane or direction with respect to the applied stress. Accordingly setting all plane indices and stress values to zero. After the Charpy impact test, the analysis of the fracture surface in terms of the Schmid factor involved setting all plane indices and stress values to zero. In FCC crystals, as the Schmid factor increases, twinning becomes the dominant deformation mechanism, while as the Schmid factor decreases, slip becomes the dominant deformation mechanism [43].

For the as-welded metal, since crystals with a high Schmid factor are mainly distributed, there is a higher possibility for twinning to be the dominant deformation mechanism and for stress to be dispersed within the crystals. However, as the PWHT temperature increases, a larger number of low Schmid factor crystals are distributed, leading to a decrease in the possibility of twinning as the major deformation mechanism.

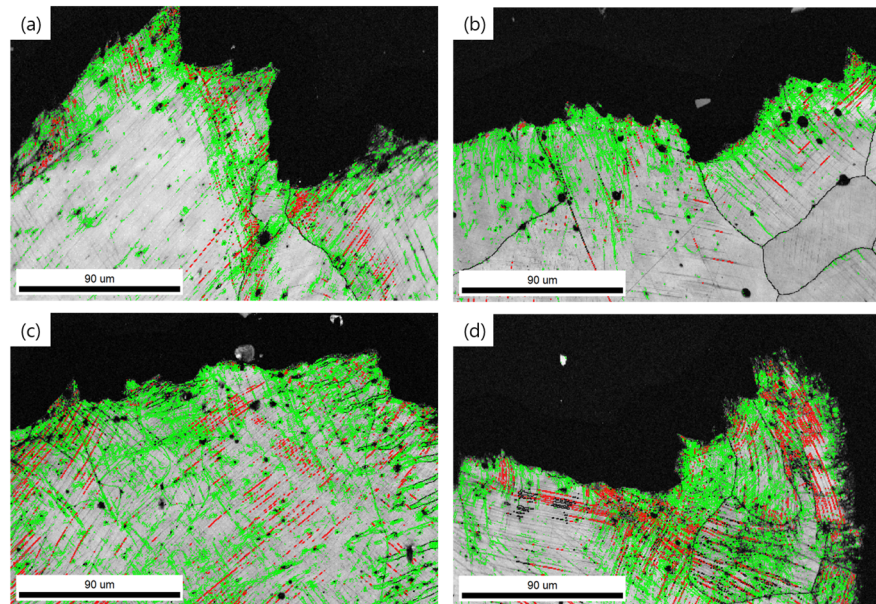


Figure 9. Fracture surface grain boundaries and $\Sigma 3$ coincidence site lattice maps of welded high manganese steel (a) as-welded weld metal and after PWHT performed at (b) 600 °C, (c) 750 °C, and (d) 900 °C.

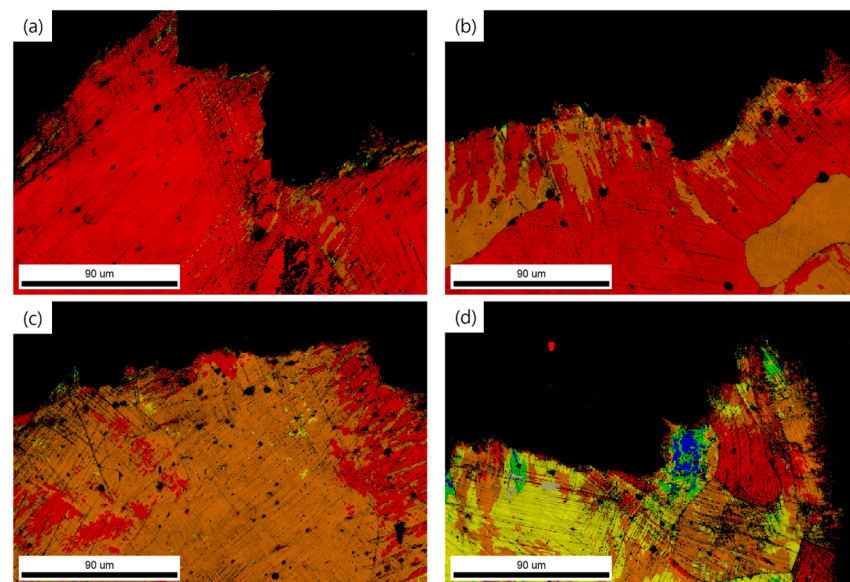


Figure 10. Fracture surface Schmid factor maps of welded high manganese steel (a) as-welded weld metal and after PWHT performed at (b) 600 °C, (c) 750 °C, and (d) 900 °C.

4. Conclusions

In this study, PWHT was conducted with the goal of improving the cryogenic impact absorbed energy of high manganese steel weld metal. The microstructure, precipitates, and SFE calculation of high manganese steel weld metal were analyzed according to the PWHT

temperature, and the correlation between the cryogenic mechanical properties was investigated through the deformation mechanism. The following conclusions were obtained:

1. As the PWHT temperature increased, the average width of the dendritic region decreased from 20.5 μm to 8.6 μm . Manganese did not fully diffuse even at high PWHT temperatures due to the slow diffusion rate.
2. The mechanical properties showed cryogenic elongation and impact absorbed energy increased by 8 J after PWHT at 900 °C, and that the strength was maintained. However, cryogenic elongation and impact absorbed energy decreased 5 J and 11 J after PWHT at 600 °C and 750 °C. All fracture surfaces were dimple fracture surfaces after the cryogenic impact test.
3. The reason for the reduction of the cryogenic impact absorbed energy was identified through the HAADF-STEM analysis, which showed the precipitation with a size of 100 nm after PWHT. The $(\text{Cr, Mn})_{23}\text{C}_6$ type carbides occurred from the interior to the grain boundaries, reducing the SFE of local areas in the depletion zone of manganese and chromium. Precipitates can easily nucleate cracks, causing cracks to propagate along the carbide particles during a fracture.
4. The reason for the increase in the cryogenic impact absorbed energy was identified through the deformation behavior of the as-welded metal, even though twinning was easily formed by a high Schmid factor, stress propagation inside the grain was not efficient, but as the PWHT temperature increased, stress propagation inside the grain became more effective. This is because the PWHT narrows the width of the dendritic region, which is the crack propagation path, and thus efficiently prevents crack propagation.

Author Contributions: S.B. designed and conducted experiments, synthesized data, and wrote the original manuscript; M.P., Experiment and Review; J.I.L. supervised, reviewed, and edited the content; S.-H.K. supervised, reviewed, edited the content analyzed the results and reviewed the manuscript. All authors have read and agreed to the published version of the manuscript.

Funding: This study has been conducted with the support of the Korea Institute of Industrial Technology as “The dynamic parameter control based smart welding system module development for the complete joint penetration weld (kitech EH-21-0003)”.

Data Availability Statement: Not applicable.

Conflicts of Interest: The authors declare no conflict of interest.

References

1. Bleck, W.; Haase, C. Physical metallurgy of high manganese steels. *Metals* **2019**, *9*, 1053. [[CrossRef](#)]
2. Haupt, M.; Müller, M.; Haase, C.; Sevsek, S.; Brasche, F.; Schwedt, A.; Hirt, G. The influence of warm rolling on microstructure and deformation behavior of high manganese steels. *Metals* **2019**, *9*, 797. [[CrossRef](#)]
3. Christian, J.W.; Mahajan, S. Deformation twinning. *Prog. Mater. Sci.* **1995**, *39*, 1–157. [[CrossRef](#)]
4. Kim, J.-S.; Jeon, J.B.; Jung, J.E.; Um, K.-K.; Chang, Y.W. Effect of deformation induced transformation of ϵ -martensite on ductility enhancement in a Fe-12 Mn steel at cryogenic temperatures. *Met. Mater. Int.* **2014**, *20*, 41–47. [[CrossRef](#)]
5. Jang, J.-M.; Kim, S.-J.; Kang, N.H.; Cho, K.-M.; Suh, D.-W. Effects of annealing conditions on microstructure and mechanical properties of low carbon, manganese transformation-induced plasticity steel. *Met. Mater. Int.* **2009**, *15*, 909–916. [[CrossRef](#)]
6. Taylor, G.I. The mechanism of plastic deformation of crystals. Part I.—Theoretical. *Proc. R. Soc. Lond. A* **1934**, *145*, 362–387.
7. Kang, J.-H.; Ingendahl, T.; von Appen, J.; Dronskowski, R.; Bleck, W. Impact of short-range ordering on yield strength of high manganese austenitic steels. *Mater. Sci. Eng. A* **2014**, *614*, 122–128. [[CrossRef](#)]
8. De Cooman, B.C.; Estrin, Y.; Kim, S.K. Twinning-induced plasticity (TWIP) steels. *Acta Mater.* **2018**, *142*, 283–362. [[CrossRef](#)]
9. Hickel, T.; Sandlöbes, S.; Marceau, R.K.; Dick, A.; Bleskov, I.; Neugebauer, J.; Raabe, D. Impact of nanodiffusion on the stacking fault energy in high-strength steels. *Acta Mater.* **2014**, *75*, 147–155. [[CrossRef](#)]
10. Hu, B.; Shen, G.; Wang, Z.; Li, S.; Wang, Y.; Luo, H. Ultrahigh tensile strength achieved in a lightweight medium Mn steel via prominent work hardening. *J. Mater. Sci. Technol.* **2023**, *145*, 156–164. [[CrossRef](#)]
11. Zheng, Z.-B.; Yang, H.-K.; Shatrava, A.; Long, J.; Wang, Y.-H.; Li, J.-X.; Zheng, K.-H. Work hardening behavior and fracture mechanisms of Fe-18Mn-1.3 C-2Cr low-density steel castings with varying proportions of aluminum alloying. *Mater. Sci. Eng. A* **2023**, *862*, 144467. [[CrossRef](#)]

12. Lindner, T.; Liborius, H.; Preuß, B.; Hanisch, N.; Schubert, A.; Lampke, T. Enhanced Abrasion Resistance of Spark Plasma Sintered and HVOF Sprayed Hadfield High Manganese Steel by Turning and Diamond Smoothing. *J. Manuf. Mater. Process.* **2022**, *6*, 48. [[CrossRef](#)]
13. Chaouadi, R.; Gerard, R. Development of a method for extracting fracture toughness from instrumented Charpy impact tests in the ductile and transition regimes. *Theor. Appl. Fract. Mech.* **2021**, *115*, 103080. [[CrossRef](#)]
14. Fu, Z.; Yang, B.; Shan, M.; Li, T.; Zhu, Z.; Ma, C.; Zhang, X.; Gou, G.; Wang, Z.; Gao, W. Hydrogen embrittlement behavior of SUS301L-MT stainless steel laser-arc hybrid welded joint localized zones. *Corros. Sci.* **2020**, *164*, 108337. [[CrossRef](#)]
15. Zhu, Z.; Liu, Y.; Gou, G.; Gao, W.; Chen, J. Effect of heat input on interfacial characterization of the butter joint of hot-rolling CP-Ti/Q235 bimetallic sheets by Laser+ CMT. *Sci. Rep.* **2021**, *11*, 10020. [[CrossRef](#)]
16. Daamen, M.; Haase, C.; Dierdorf, J.; Molodov, D.A.; Hirt, G. Twin-roll strip casting: A competitive alternative for the production of high-manganese steels with advanced mechanical properties. *Mater. Sci. Eng. A* **2015**, *627*, 72–81. [[CrossRef](#)]
17. Lan, P.; Zhang, J. Thermophysical properties and solidification defects of Fe–22Mn–0.7 C TWIP steel. *Steel Res. Int.* **2016**, *87*, 250–261. [[CrossRef](#)]
18. Park, M.; Kang, M.; Park, G.-W.; Jang, G.; Kim, B.; Kim, H.C.; Jeon, J.B.; Kim, H.; Kwon, S.-H.; Kim, B.J. The effects of post weld heat treatment for welded high-Mn austenitic steels using the submerged arc welding method. *J. Mater. Res. Technol.* **2022**, *18*, 4497–4512. [[CrossRef](#)]
19. Hamada, A.; Ali, M.; Ghosh, S.; Jaskari, M.; Keskitalo, M.; Järvenpää, A. Mechanical performance and formability of laser-welded dissimilar butt joints between medium-Mn stainless steel and high-strength carbon steel. *Mater. Sci. Eng. A* **2022**, *831*, 142200. [[CrossRef](#)]
20. Hamada, A.; Ghosh, S.; Ali, M.; Jaskari, M.; Järvenpää, A. Studying the strengthening mechanisms and mechanical properties of dissimilar laser-welded butt joints of medium-Mn stainless steel and automotive high-strength carbon steel. *Mater. Sci. Eng. A* **2022**, *856*, 143936. [[CrossRef](#)]
21. Chen, Y.; Sun, S.; Zhang, T.; Zhou, X.; Li, S. Effects of post-weld heat treatment on the microstructure and mechanical properties of laser-welded NiTi/304SS joint with Ni filler. *Mater. Sci. Eng. A* **2020**, *771*, 138545. [[CrossRef](#)]
22. Tewary, N.; Ghosh, S.; Mandal, A.; Chakrabarti, D.; Chatterjee, S. Effect of annealing on the microstructure, texture and mechanical properties of a dual-phase ultrahigh-strength TWIP steel. *Metall. Mater. Trans. A* **2020**, *51*, 4483–4498. [[CrossRef](#)]
23. Chen, J.; Ren, J.-k.; Liu, Z.-y.; Wang, G.-d. Interpretation of significant decrease in cryogenic-temperature Charpy impact toughness in a high manganese steel. *Mater. Sci. Eng. A* **2018**, *737*, 158–165. [[CrossRef](#)]
24. Maslak, M.; Pazdanowski, M.; Stankiewicz, M.; Wassilkowska, A.; Zajdel, P.; Zielina, M. Impact fracture surfaces as the indicators of structural steel post-fire susceptibility to brittle cracking. *Materials* **2023**, *16*, 3281. [[CrossRef](#)]
25. Heo, N.-H. Theory of nonequilibrium segregation in an FeMnNi ternary alloy and a ductile-brittle-ductile transition. *Acta Mater.* **1996**, *44*, 3015–3023. [[CrossRef](#)]
26. Liu, Z.; Gao, X.; Xiong, M.; Li, P.; Rao, D.; Misra, R. Recrystallization Behavior and Microstructure Evolution in High-Manganese Austenitic Steel. *Steel Res. Int.* **2021**, *92*, 2100029. [[CrossRef](#)]
27. Pahlavani, M.; Marzbanrad, J.; Rahmatabadi, D.; Hashemi, R.; Bayati, A. A comprehensive study on the effect of heat treatment on the fracture behaviors and structural properties of Mg-Li alloys using RSM. *Mater. Res. Express* **2019**, *6*, 076554. [[CrossRef](#)]
28. Olson, G.; Cohen, M. Stress-assisted isothermal martensitic transformation: Application to TRIP steels. *Metall. Trans. A* **1982**, *13*, 1907–1914. [[CrossRef](#)]
29. Lee, Y.-K.; Choi, C. Driving force for $\gamma \rightarrow \epsilon$ martensitic transformation and stacking fault energy of γ in Fe-Mn binary system. *Metall. Mater. Trans. A* **2000**, *31*, 355–360. [[CrossRef](#)]
30. Li, L.; Hsu, T. Gibbs free energy evaluation of the fcc (γ) and hcp (ϵ) phases in Fe-Mn-Si alloys. *Calphad* **1997**, *21*, 443–448. [[CrossRef](#)]
31. Curtze, S.; Kuokkala, V.-T.; Oikari, A.; Talonen, J.; Hänninen, H. Thermodynamic modeling of the stacking fault energy of austenitic steels. *Acta Mater.* **2011**, *59*, 1068–1076. [[CrossRef](#)]
32. Allain, S.; Chateau, J.-P.; Bouaziz, O.; Migot, S.; Guelton, N. Correlations between the calculated stacking fault energy and the plasticity mechanisms in Fe–Mn–C alloys. *Mater. Sci. Eng. A* **2004**, *387*, 158–162. [[CrossRef](#)]
33. Ferreira, P.; Müllner, P. A thermodynamic model for the stacking-fault energy. *Acta Mater.* **1998**, *46*, 4479–4484. [[CrossRef](#)]
34. Dinsdale, A.T. SGTE data for pure elements. *Calphad* **1991**, *15*, 317–425. [[CrossRef](#)]
35. Dumay, A.; Chateau, J.-P.; Allain, S.; Migot, S.; Bouaziz, O. Influence of addition elements on the stacking-fault energy and mechanical properties of an austenitic Fe–Mn–C steel. *Mater. Sci. Eng. A* **2008**, *483*, 184–187. [[CrossRef](#)]
36. Ishida, K.; Nishizawa, T. Effect of alloying elements on stability of epsilon iron. *Trans. Jpn. Inst. Met.* **1974**, *15*, 225–231. [[CrossRef](#)]
37. Rahman, K.; Vorontsov, V.; Dye, D. The effect of grain size on the twin initiation stress in a TWIP steel. *Acta Mater.* **2015**, *89*, 247–257. [[CrossRef](#)]
38. Hamada, A.; Karjalainen, L.; Puustinen, J. Fatigue behavior of high-Mn TWIP steels. *Mater. Sci. Eng. A* **2009**, *517*, 68–77. [[CrossRef](#)]
39. Rahmatabadi, D.; Tayyebi, M.; Najafizadeh, N.; Hashemi, R.; Rajabi, M. The influence of post-annealing and ultrasonic vibration on the formability of multilayered Al5052/MgAZ31B composite. *Mater. Sci. Technol.* **2021**, *37*, 78–85. [[CrossRef](#)]
40. Kaneko, K.; Fukunaga, T.; Yamada, K.; Nakada, N.; Kikuchi, M.; Saghi, Z.; Barnard, J.S.; Midgley, P.A. Formation of M23C6-type precipitates and chromium-depleted zones in austenite stainless steel. *Scr. Mater.* **2011**, *65*, 509–512. [[CrossRef](#)]

41. Ramkumar, K.D.; Mulimani, S.S.; Ankit, K.; Kothari, A.; Ganguly, S. Effect of grain boundary precipitation on the mechanical integrity of EBW joints of Inconel 625. *Mater. Sci. Eng. A* **2021**, *808*, 140926. [[CrossRef](#)]
42. Gigacher, G.; Krieger, W.; Scheller, P.R.; Thomser, C. Non-Metallic Inclusions in High-Manganese-Alloy Steels. *Steel Res. Int.* **2005**, *76*, 644–649. [[CrossRef](#)]
43. Zhang, W.; Gao, Y.; Xia, Y.; Bei, H. Indentation Schmid factor and incipient plasticity by nanoindentation pop-in tests in hexagonal close-packed single crystals. *Acta Mater.* **2017**, *134*, 53–65. [[CrossRef](#)]

Disclaimer/Publisher’s Note: The statements, opinions and data contained in all publications are solely those of the individual author(s) and contributor(s) and not of MDPI and/or the editor(s). MDPI and/or the editor(s) disclaim responsibility for any injury to people or property resulting from any ideas, methods, instructions or products referred to in the content.